ORIGINAL ARTICLE

MOPSO process parameter optimization in ultrasonic vibration-assisted grinding of hardened steel

Qiang Huang[1] · Biao Zhao[1] ⬤ · Yutong Qiu[1] · Yang Cao[1] · Yucan Fu[1] · Qingliang Chen[2] · Menglan Tang[3] · Mingming Deng[3] · Guoliang Liu[3] · Wenfeng Ding[1]

Abstract

Ultrasonic vibration-assisted grinding (UVAG) is a highly effective technique for improving the grindability of difficult-to-cut materials, making it widely applicable in various industrial fields. However, the conventional optimization of grinding parameters necessitates extensive experimental analyses and is susceptible to converging towards a local optimum. A multiobjective particle swarm optimization (MOPSO) model is developed in this study to predict grinding forces and surface roughness based on comparative experiments between UVAG and conventional grinding. Optimized process parameters are utilized to perform experiments on ultrasonic vibration-assisted profile grinding, resulting in a reduction of 20.51% and 18.91% in tangential and normal grinding forces, respectively, as well as a decrease of 9.47% in ground surface roughness. In addition, UVAG can maintain the sharpness of grinding wheels. The MOPSO algorithm yields a Pareto solution set comprising 15 noninferior solutions, indicating that superior surface roughness is achieved by increasing wheel speed and cutting depth while decreasing feed speed. The ultrasonic vibration-assisted profile grinding process enables the formation of workpieces with exceptional shape accuracy and high surface quality, while also optimizing machining parameters.

Keywords Ultrasonic vibration-assisted grinding · MOPSO · Grinding force · Surface roughness integrity

1 Introduction

In recent years, ultrasonic vibration-assisted processing has shown significant potential over conventional processing in the machining process of difficult-to-cut materials (e.g., superalloys [1], ceramic materials [2], composites [3], and hardened materials [4]). In particular, ultrasonic vibration-assisted processing has exhibited deformation force decrease [5, 6], processing temperature increase [7, 8], and surface quality increase [9, 10]. Zhao et al. [11] reported that ultrasonic vibration-assisted processing has been widely used in grind processing due to its ability to improve the material removal rate greatly. However, Cao et al. [12] reported that the excellent performance of ultrasonic vibration-assisted grinding (UVAG) demonstrated opposite results under different machining parameters owing to the complexity of processes. Meanwhile, different parameter optimization methods have proved to be a great improvement in the optimization of conventional grinding parameters [13, 14]. The optimizing parameters of the UVAG process, based on ground surface quality, machining efficiency, or production cost, exhibit a broad potential for application.

Process parameter optimization and decision-making, as effective methods for process control, have garnered significant attention both domestically and internationally due to their utilization of experimental and analytical techniques. Ren et al. [15] used the response surface methodology as an optimization method for high-speed grinding parameters to reach a higher anti-fatigue performance of 20CrMnTi steel workpieces. Wang et al. [16] optimized grinding parameters and cooling conditions on the basis of Taguchi tests and achieved the highest comprehensive benefits of technology. Additionally, a set of economic and environmental benefit models were established, encompassing costs, production rates, and carbon

✉ Biao Zhao
zhaobiao@nuaa.edu.cn

[1] National Key Laboratory of Science and Technology On Helicopter Transmission, Nanjing University of Aeronautics and Astronautics, Nanjing 210016, China

[2] AVIC Cheng'du Aircraft Industrial (Group) Co., LTD, Chengdu 610092, China

[3] AECC Zhongchuan Transmission Machinery Co., LTD, Changsha 410200, China

dioxide emissions. Typically, grinding parameters are selected based on the grinding mechanism to meet production requirements while controlling expenses. However, when faced with conflicting production demands, experimental methods tend to converge towards local optima. The analytical method is increasingly favored over the experimental method due to its powerful global solving capabilities.

The multi-objective optimization algorithm effectively predicts and solves the optimal parameter settings by establishing an optimal model of the parameters between the analytical objectives and the constraints [17, 18]. Khan et al. [19] carried out a multi-objective optimization based on the grey-Taguchi method for the mathematical model of grinding temperature, normal grinding force, and ground surface quality in machining AISI D2 steels under different cooling modes. They also proposed the optimal parameter settings to optimize the system performance. Zhang et al. [20] conducted experimental trials in grinding 20CrMnTi hardened steels and detected ground surface quality under different grinding parameters. They found that the improved Pareto optimization algorithm could accurately predict the surface quality and effectively solve the optimization problem between the ground surface quality and grinding efficiency. Zhou et al. [21] established two neural network models to precast and then optimize force in the creep feed grinding of a titanium matrix composite. The backpropagation (BP) neural network model optimized using the genetic algorithm model was superior to the traditional regression and BP models in view of the prediction accuracy. However, the influence of the machining parameters on the processing results is more complex due to the influence of ultrasonic vibrations in ultrasonic grinding [3, 13]. Therefore, the optimization of ultrasonic grinding by multi-objective optimization algorithm (i.e., multiobjective particle swarm optimization, MOPSO) can effectively solve the problem that the optimal parameters for machining in ultrasonic processing depend on a large number of experiments.

In this study, comparison grinding experiments were initially conducted to obtain optimized model coefficients through regression analysis. Subsequently, a MOPSO model was established on the Pareto optimal frontier and developed to optimize process parameters with grinding forces and ground surface roughness as optimization objectives. Finally, the optimized machining parameters were utilized to achieve high-quality surface profile grinding.

2 Particle swarm optimization based on Pareto optimal solution (MOPSO)

Particle swarm algorithms originated from the study of bird flock predation behavior and aim to achieve optimal solutions through collaborative group sharing and information exchange [12]. To address multiobjective optimization problems, Coello et al. [22] proposed a widely used MOPSO based on particle optimal solution, which is characterized by its simplicity in calculation, convenience in parameter setting, and fast convergence speed.

The MOPSO algorithm continuously updates the Pareto solution set and iteratively compares it with the Pareto front under machining constraints to search for grinding parameters [23]. Firstly, based on the general empirical formula and experimental results in Sect. 2.1, an optimization model and normal force (F_n) constraints are established and surface roughness (R_a) can be established as follows [24]:

$$\begin{cases} \text{Normal grinding force}: F(x) = K_f x_1^{\lambda_1} x_2^{\lambda_2} x_3^{\lambda_3} \\ \text{Surface roughness}: R(x) = R_f x_1^{\gamma_1} x_3^{\gamma_3} \end{cases}$$
$$f(x) = \{F(x), R(x)\}$$
$$\Rightarrow \text{Minimum model}: \min\{f(x)\} = \min\{F(x), R(x)\} \text{ for all } x \in x^D$$
$$(1)$$

$$\text{s.t.} \begin{cases} x_p = (x_1, x_2, x_3)^T \\ v_{s1} \le x_1 \le v_{s2} \\ v_{w1} \le x_2 \le v_{w2} \\ a_{p1} \le x_3 \le a_{p2} \\ \frac{x_2 \cdot x_3}{60} \ge Q_w \end{cases} \quad (2)$$

where x_1, x_2, and x_3 are the grinding speed, feed speed, and depth of cut, respectively. K_f, λ_1, λ_2, λ_3, R_f, γ_1, γ_2, and γ_3 are the empirical formula coefficients obtained by regression analysis of the experimental result data. Min $f(x)$ is the model for finding a Pareto set, and v_s, v_w a_p, and Q_w are the machining constraint intervals.

Second, according to the MOPSO algorithm, each particle contains the following information:

  (i) Current speed v_p and position x_p
 (ii) Current objective function values (fitness values) $f(x_p)$
(iii) Historic best location $x_{p\text{-best}}$
(iv) Historic best objective function fitness values $f(x_{p\text{-best}})$

The solution space search process involves calculating the current particle fitness and updating its position and velocity during each iteration based on inertia and historical optimal positions.

$$\begin{cases} v_p^{k+1} = w v_p^k + c_1 r_1 (x_{p-best} - x^k) + c_2 r_2 (x_{g-best} - x^k) \\ x_p^{k+1} = x_p^k + v_p^{k+1} \end{cases} \quad (3)$$

where v_p^{k+1} and x_p^{k+1} are the velocity and position of the particle after the update, respectively; r_1 and r_2 are random numbers between 0 and 1; w is the inertia weight factor; c_1 and c_2 are constants; k is the number of current iterations;

and $x_{g\text{-best}}$ is the global optimum position of the particle swarm. Figure 1 shows the flowchart of the MOPSO model.

3 Experimental environment

3.1 Surface grinding setup

In this study, a Blohm Profimat MT-408 surface grinder was employed for comparative experiments under UVAG and conventional grinding (CG) processes (Fig. 2). White corundum abrasive wheels (WA80F6V45m) with a dimension of 380 mm × 20 mm × 127 mm were used as material removal units because of their suitability for carbon steel and hardened steel processing [11]. For the ultrasonic system, an ultrasonic generator equipped with an output power (maximum 500 W) was utilized to produce electric energy, and the tiny vibration of the transducer was amplified through the horn. In this case, the tangential range vibration could be produced on the center zone of the porous platform, as shown in Fig. 1b [12]. The force measurement system consisted of a three-phase piezoelectric dynamometer (Kistler 9253B) and a multichannel charge amplifier (Kistler 5080A). The dimensions of the workpiece were 30 mm × 10 mm × 12 mm (L × W × H), and the hardness was in the range
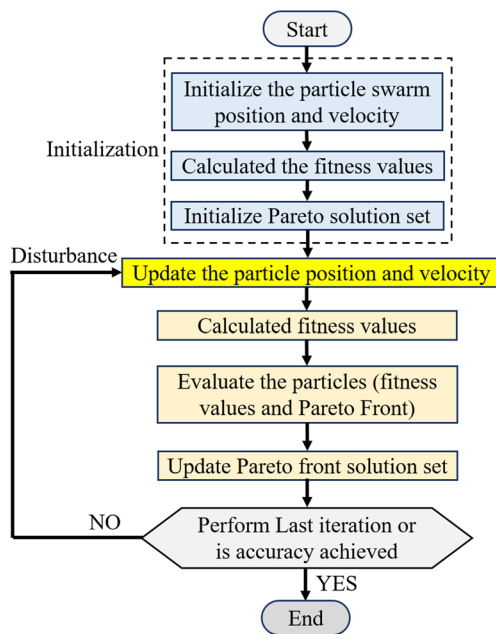
of HRC 60–62 within 2 mm depth. Tables 1 and 2 present the chemical element composition and mechanical capacity of the hardened GCr15 steel, respectively. Table 3 presents the experimental parameters employed in surface grinding, wherein a wheel dresser was utilized to dress the grinding wheel and maintain its potential for cutting the workpiece post-experiment. The trimming parameters included a grinding speed of $v_{st} = 20$ m/s, a feed rate of $v_{wt} = 200$ mm/min, and a cutting depth of $a_{pt} = 200$ μm. Compressed air was injected into a sealed shell to maintain the stable temperature inside the UVAG system.

3.2 Profile grinding experiments on curved parts

The profile grinding setup and workpiece are depicted in Fig. 3. Initially, the GCr15 workpiece's surface profile was machined with a 0.2 mm allowance through wire-electrode cutting processes, followed by heat treatment (carburization at 920 ℃ and oil cold quenching at 850 ℃). Finally, the hardened GCr15 steel profile was machined under the same surface grinder as described in Sect. 2.1. Meanwhile, the white corundum abrasive wheel was dressed using a diamond disc wheel at a fixed dressing speed of 20 m/s and feed speed of 1.3 mm/min. The shape of the abrasive wheels was tailored to match the target profile of the workpiece, as illustrated in Fig. 3b. The same UVAG devices described in Sect. 2.1 were utilized, with the curved workpiece securely fastened onto the porous plate center of the UVAG system. To enhance the validity of machining parameter optimization, both surface grinding and profile grinding were employed for verification [25]. Subsequently, experiments were conducted using the optimized parameters in Sect. 3.3 as presented in Table 4. Prior to each grinding experiment, the profile wheel was dressed with a diamond dish wheel.

3.3 Characterization methods

Prior to grinding experiments, the vibration amplitude and frequency of the workpiece were calibrated using a laser

Table 2 Mechanical capacity of GCr15

Yield strength $\sigma_{0.2}$ (MPa)	Tensile strength σ_b (MPa)	Elastic modulus E (GPa)	Density ρ (g/cm³)	Thermal conductivity k (W/(m·K))	Hardness (HRC)
1394	1748	210	7.83	46.6	62

Fig. 1 Flowchart of the MOPSO model

Table 1 Chemical element composition of GCr15 (%)

Element	C	Si	Mn	P	S	Cr	Ni	Mo	Fe
Component/%	1.03	0.227	0.353	0.007	0.003	1.46	0.015	0.0096	Balance

Table 3 Grinding parameters

Contents	Values	
Machine tool	Blohm Profimat surface grinder MT-408	
Abrasive wheel	White alundum wheel (WA80F6V45M)	
Grinding mode	Down grinding	
Cooling condition	5% emulsified, pressure at 0.5 MPa	
Frequency f (kHz)	19.6	
Amplitude A (μm)	6	
Wheel speed v_s (m/s)	15, 20, 25, 30	$v_w = 8$ m/min and $a_p = 15$ μm
Feed speed v_w (m/min)	4, 6, 8, 10	$v_s = 25$ m/s and $a_p = 15$ μm
Cutting depth a_p (μm)	10, 15, 20, 25	$v_s = 25$ m/s and $a_p = 15$ μm

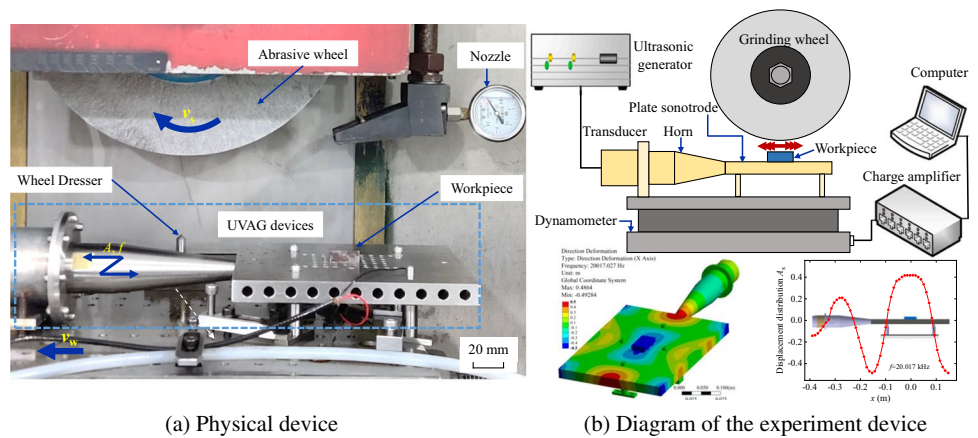**Fig. 2** Schematic of the surface grinding experiment

(a) Physical device   (b) Diagram of the experiment device

Fig. 3 Diagram of the profile grinding setup and workpiece

(a) Main view of the profile grinding experimental setup   (b) Right view of the experimental setup and workpiece parameter
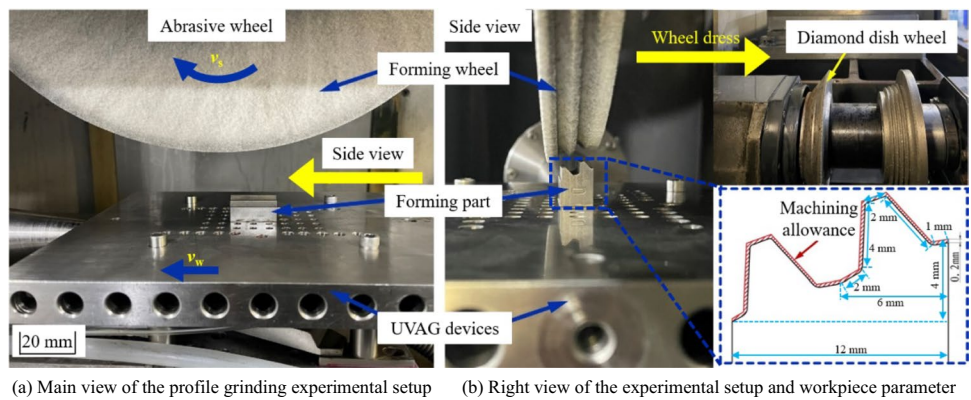
Table 4 Parameters for surface grinding processes

Wheel speed v_s (m/s)	Workpiece speed v_w (m/min)	Depth of cut a_p (μm)	Vibration frequency f (kHz)	Ultrasonic amplitude A (μm)
30	6	25	19.6	6

Doppler vibrometer (LV-S01, SOPTOP). Three points on the end face were randomly selected to measure, and the sampling frequency was fixed at 480 kHz. Hence, a stable ultrasonic amplitude (A) of 6 μm was generated in the

workpiece when the ultrasonic power supply was 35% and the frequency was fixed at 19.60 kHz.

The grinding force measurement system comprised a Kistler 9253B three-phase piezoelectric dynamometer and a Kistler 5080A multichannel charge amplifier, which collected and amplified electrical signals. The average value of the grinding force was calculated as the single value of the forces exerted during the time period between wheel contact with and separation from the workpiece. Following each grinding process, the surface roughness profile Ra of the machined workpiece was measured using a handheld

MAHR M2 roughness meter. Based on GB/1031 standards and practical experience, the ground surface roughness during grinding ranged from 0.1 to 2 μm with a sampling length of 0.8 mm. Three points were selected along the grinding direction at the beginning, middle, and end of grinding for measurement in a direction perpendicular to that of grinding.

The workpiece surface topography was examined post-forming grinding. Initially, the machined workpiece was cleaned with 75% alcohol using an ultrasonic cleaning machine. Subsequently, the curved end face and surface were scrutinized utilizing a three-dimensional video microscope (HK-7700) and scanning electron microscope (SEM, Quanta 200). To investigate chips, coolant was collected during CG and UVAG experiments. Afterward, the collected coolant was dried using a dryer and cleaned with 75% alcohol, and SEM was used to observe the chips that adhered to the conductive tape.

4 Results and discussion

4.1 Grinding forces and force ratio

Figure 4 illustrates the impact of processing parameters on normal force (F_n) and tangential force (F_t) during grinding of a hardened steel surface. The results indicate that UVAG exhibits lower normal and tangential forces compared

to CG across all experimental grinding conditions. Seen from Fig. 4a, the normal and tangential forces are reduced from 193.56 to 130.65 N and from 97.22 to 67.97 N in CG, respectively, and from 177.80 to 112.38 N and from 85.88 to 58.70 N in UVAG, respectively, as the wheel speed (v_s) rises from 15 to 30 m/s at a feed speed v_w of 8 m/min and a cut depth a_p of 15 μm. Ultrasonic vibration reduces the tangential grinding forces by up to 13.64% and the normal grinding forces by up to 14.08% in UVAG compared with those in CG. However, the difference in forces between CG and UVAG changes minimally with increasing wheel speed, suggesting that grinding speed is not sensitive to the effect of ultrasonic vibration on grinding forces, as reported by Wang et al. [10] and Cao et al. [12]. As the workpiece speed of v_w increases from 4 to 10 m/min, F_n of CG increases from 88.67 to 154.69 N, and F_t of CG increases from 49.63 to 77.96 N, as shown in Fig. 4b. The tendency of F_n and F_t in UVAG is similar to that in the CG process, but F_n and F_t are always lower by 16.76 and 10.18 N, respectively in contrast to those in CG.

The effect of ultrasonic vibration in reducing grinding forces decreases with increasing workpiece speed, indicating that the reduced workpiece feed more satisfies UVAG, as stated by Huang et al. [2] and Zhao et al. [11]. The reason is that the ultrasonic vibration increases the relative feed speed more obviously at a small feed speed [26]. As illustrated in

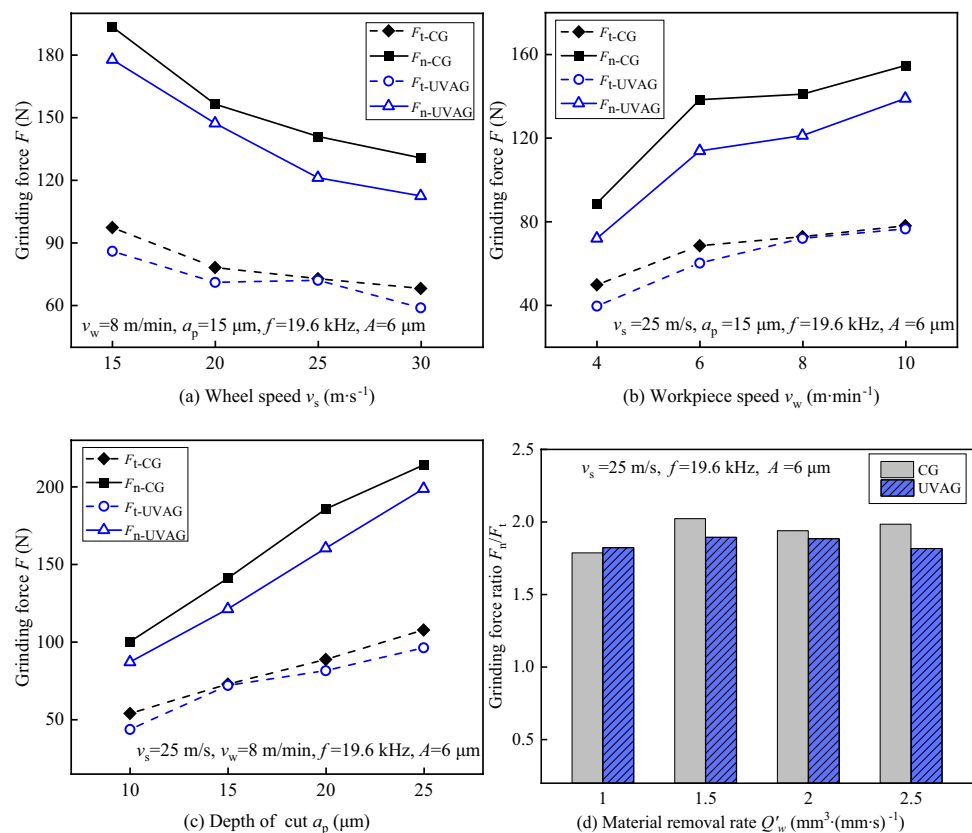Fig. 4 Grinding forces and force ratio with different grinding parameters

Fig. 4c, F_n and F_t of CG and UVAG rise with the increase in cut depth a_p, i.e., from 100.04 to 214.05 N and from 53.74 to 107.57 N in CG, respectively, and from 86.92 to 198.76 N and from 43.49 to 96.14 N in UVAG, respectively. As the material removal rate increases, the grinding force also increases significantly; therefore, more energy is required to remove the material. UVAG demonstrates lower values of F_n and F_t by 14.08% and 19.07% than those of CG, respectively. This phenomenon implies that the employment of ultrasonic vibration contributes to the reduction in grinding forces owing to the ultrasonic softening and lubrication effects [27]. Meanwhile, the impact of ultrasonic vibration increases the microbreakage of the wheel grain and maintains the sharpness of the grain cutting edge during the grinding process [28]. Figure 4d presents the grinding force ratio with the different material removal rates (Q'_w) applied in CG and UVAG.

$$Q'_W = a_v v_w \tag{4}$$

As Q'_w rises from 1 to 2.5 mm³/(mm·s), the force ratio varies in the range of 1.79–2.02 during CG, while the UVAG force ratio on a scale of 1.82–1.89 is more stable. UVAG can effectively reduce wheel wear and maintain sharpness consistently, providing important evidence of reduced grinding forces. The microshattering of abrasive grains under ultrasonic impact creates new cutting edges, ensuring the constant sharpness of the grinding wheel.

Specific grinding energy e_s plays a vital role in estimating the power for removing materials, which is calculated from grinding forces and machining parameters [29]. The e_s of hardened surfaces under CG and UVAG can be expressed by material removal rate (Q'_W), as shown below [30]:

$$CG : e_s = 173.74 Q'^{-0.314}_W \tag{5}$$

$$UVAG : e_s = 122.40 Q'^{-0.170}_W \tag{6}$$

Seen from Fig. 5, the specific grinding energy decreases as Q'_w increases under different grinding conditions. Under the grinding condition of $Q'_w = 1$ mm³/(mm·s), the specific grinding energy in CG and UVAG is 124.08 J/mm³ and 100.14 J/mm³, respectively. The proportion of cutting processes rapidly increases with ultrasonic vibration; thus, the energy consumption caused by sliding and ploughing processes decreases. In this case, the specific grinding energy in UVAG can be reduced compared with that in CG under the same condition. This is because ultrasonic vibration leads to thicker and shorter chips at a low material removal rate [31]. When the material removal rate Q'_w increases from 1 to 2.5 mm³/(mm·s), e_s values in CG and UVAG processing are reduced by 26.77% and 10.24%, respectively, indicating that
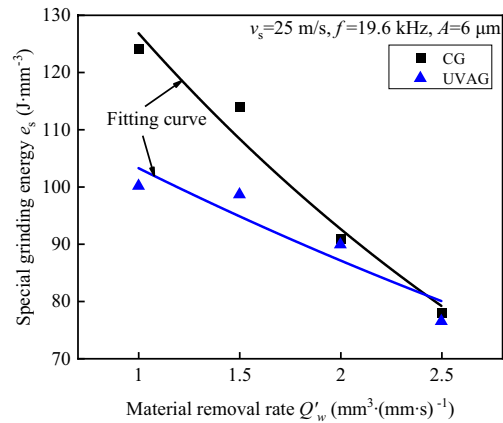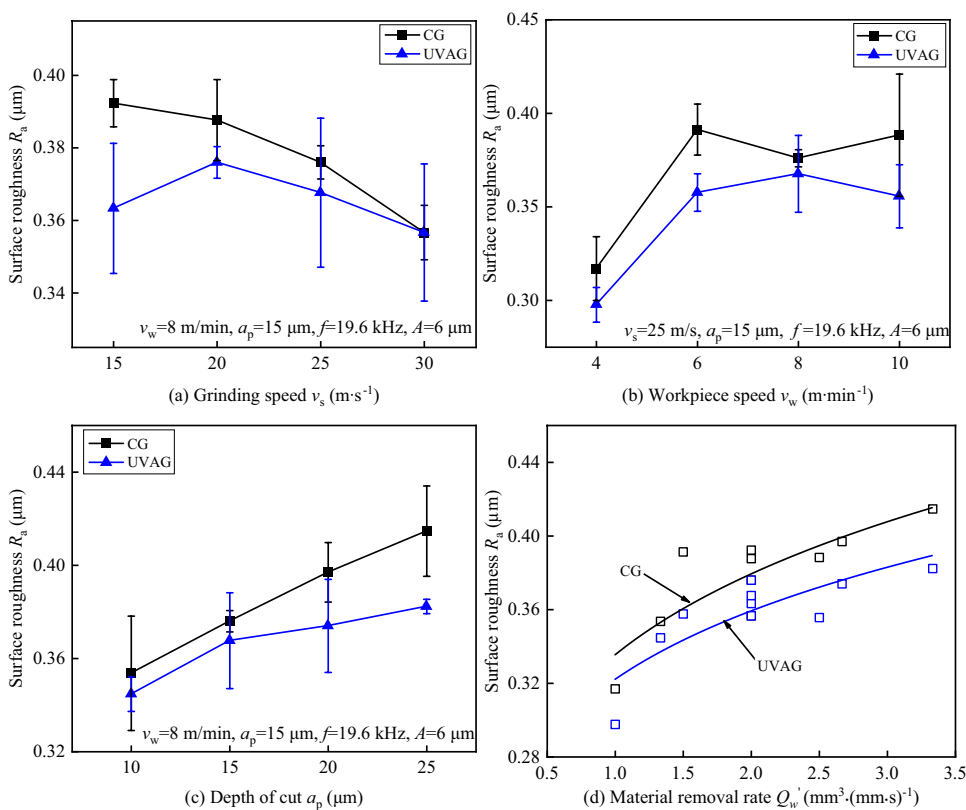

Fig. 5 Effects of the material removal rate on specific grinding energy

the energy consumption per unit decreases as the material removal rate increases owing to the size effect [32].

4.2 Ground surface roughness

Surface roughness is an important component of surface quality and plays a key role in machining accuracy and fatigue life [33]. Figure 6 shows the influence of machining parameters on the surface roughness profile R_a during CG/UVAG processes. With all processing parameters, R_a of UVAG is always less than that of CG. In Fig. 6a, when the wheel speed (v_s) rises from 15 to 30 m/s with constant values $v_w = 7.5$ m/min and $a_p = 15$ μm, the surface roughness R_a decreases in the range of 0.392–0.357 μm under CG and in the range of 0.376–0.357 μm under UVAG. That is, the ultrasonic vibration reduces the surface roughness by up to 9.47% compared with CG (Fig. 6a). As the v_w value rises from 4 m/min to 10 m/min, with $v_s = 25$ m/s and $a_p = 15$ μm, the R_a value of CG rises from 0.317 to 0.389, by 22.71%, and that of UVAG increases from 0.298 to 0.356, by 19.46%, as depicted in Fig. 6b. When a_p rises from 10 to 25 μm, R_a of CG increases by 17.56% from 0.354 to 0.415, and that of UVAG increases by 10.72% from 0.345 to 0.382 (Fig. 6c). UVAG shows the most significant improvement in surface integrity at 25 μm cutting depth because the ultrasonic vibration allows the grinding wheel to undergo microbreakage while retaining the sharpness as the cutting depth increases. As the material removal rate increases from 1 to 3.33 mm³/(mm·s), the CG surface roughness increases from 0.317 to 0.415 μm (i.e., an increase of 30.9%), while the UVAG surface roughness is always lower than the CG value (i.e., up to 9.47%). Surface roughness is related to the height of the material remaining on the machined surface [31]. The repeated

Fig. 6 Effects of grinding parameters on ground surface roughness

(a) Grinding speed v_s (m·s^{-1})

(b) Workpiece speed v_w (m·min^{-1})

(c) Depth of cut a_p (μm)

(d) Material removal rate $Q_w{}'$ (mm^3·(mm·s)$^{-1}$)

ironing effect of the grinding wheel on the processed surface by ultrasonic vibration reduces the residual height on the surface [31], resulting in better R_a of UVAG.

4.3 Parameter optimization

From the normal grinding force data obtained from 10 sets of grinding tests, 9 sets were selected as sample data. After conducting statistical regression analysis, empirical equations for CG and UVAG were derived as follows:

$$CG : F_n = 26.482 v_s^{-0.560} v_w^{0.560} a_p^{0.840} \tag{7}$$

$$UVAG : F_n = 26.616 v_s^{-0.681} v_w^{0.712} a_p^{0.895} \tag{8}$$

Similarly, with surface roughness as the target, the empirical equations for CG and UVAG are obtained as follows:

$$CG : R_a = 0.222 v_s^{-0.106} v_w^{0.190} a_p^{0.176} \tag{9}$$

$$UVAG : R_a = 0.196 v_s^{-0.047} v_w^{0.214} a_p^{0.177} \tag{10}$$

Table 5 shows the adjusted determination coefficient (Adj. R^2) and significance F of the above regression equations. The Adj. R^2 of different regression equations are all greater than 0.8, which is very close to 1. Therefore, each

characteristic parameter is meaningful. The significance F indicates that the lowest confidence of R_a regression equation of CG is 97.92%, and the grinding force is 99.99%. Thus, these regression equations can be used for later analysis.

As presented in Table 6, the last three sets of experimental parameters were incorporated into the empirical model, yielding calculated values that deviated by no more than 5% from their corresponding experimental counterparts. This outcome attests to the reliability of our established model for normal grinding forces and ground surface roughness profiles. Notably, we observed a smaller error in CG compared to UVAG, which may be attributed to random abrasive grain fragmentation induced by ultrasonic vibration.

The empirical equations, namely Eqs. 6–9, are incorporated into Eq. 1 while the boundary conditions are integrated into Eq. 2. The programming process is executed using data processing software, setting the inertia weight factor $w = 0.5$, the constant values $c_1 = 2$ and $c_2 = 2$, and the maximum

Table 5 Adjusted determination coefficient (Adj. R^2) and significance F of regression analysis

	F_n		R_a	
	CG	UVAG	CG	UVAG
Adj. R^2	0.917	0.954	0.859	0.804
Significance F	3.63×10^{-4}	6.39×10^{-5}	0.0207948	0.00685

Table 6 Comparative results between the calculated and experimental values of the formula

Parameters	Value	F_n/N		R_a/μm	
		CG	UVAG	CG	UVAG
$v_s = 25$ m/s $v_w = 8$ m/min $a_p = 15$ μm	Calculated	142.67	125.42	0.377	0.361
	Experimental	140.98	121.13	0.376	0.368
	Error/%	1.20	3.54	0.26	1.90
$v_s = 30$ m/s $v_w = 6$ m/min $a_p = 25$ μm	Calculated	167.08	142.46	0.383	0.357
	Experimental	162.24	143.08	0.376	0.344
	Error/%	2.90	0.435	1.82	3.64
$v_s = 15$ m/s $v_w = 4$ m/min $a_p = 10$ μm	Calculated	90.10	75.36	0.325	0.304
	Experimental	94.57	78.32	0.315	0.305
	Error/%	4.97	3.93	3.08	0.33

number of iterations $k \leq 300$. The optimization results are listed in Fig. 7. The particles are observed to continuously move towards the lower left corner of Fig. 7, indicating a direction of lower surface roughness and grinding forces. The Pareto solution comprises 15 sets of noninferior solutions, with the Pareto optimal frontier being depicted in the right panel. The optimized wheel speed is determined as the maximum boundary value, signifying that an increase in grinding speed yields superior results in reducing grinding forces and enhancing surface quality. Meanwhile, increasing the cutting depth while decreasing the workpiece speed can effectively reduce surface roughness. Therefore, the MOPSO algorithmic model is consistent with grinding mechanisms and useful for optimizing machining processes.
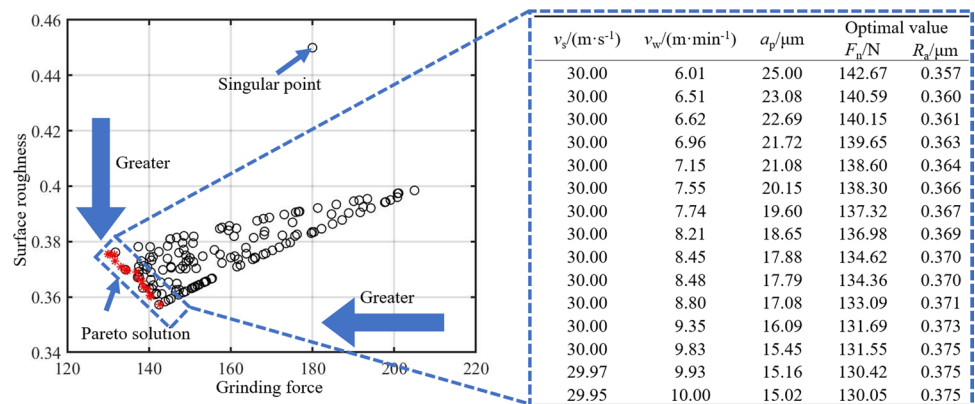
4.4 Ground surface and chip morphologies

The surface morphology of the workpiece end face (cutout surface) after profile grinding with constant processing values of $v_s = 30$ m/s, $v_w = 6$ m/min, and $a_p = 25$ μm is presented in Fig. 8. Various defects such as material adhesion and micro-fracture are observed on the end face for CG, whereas no defects are evident for UVAG. Clear

edges and no extruded burrs in the root area of the curved part in profile grinding of CG and UVAG are observed in Fig. 8a. The end face in the area of crest I under profile grinding of CG exhibits material adherence due to the thinner chips at the crest during profile grinding [35], which hinders heat dissipation during machining. The accumulation of heat generated during grinding leads to the cold welding of residual material from thinner edge chips on the end face. Micro-fractures are observed in the crest II area of the tooth during profile grinding with CG, indicating a decrease in accuracy of the grinding wheel shape at crest II due to abrasive particles resulting from higher grinding temperatures in this region. On the contrary, as depicted in Fig. 8b, neither of these defects manifest at crest I and crest II during UVAG profile grinding, resulting in exceptional performance with respect to dimensional accuracy and surface profile of formed parts. The vibration cuts the workpiece surface, leading to shorter chips and more chip breakage than that observed in CG; thusly, no chip adhesion occurs, as evidenced by Fig. 9. The average chip length (L_{CGmax}) is 493 μm and the average width (W_{Cgmax}) is 25 μm under CG, while the average chip length ($L_{UVAGmax}$) is 164 μm and the average width ($W_{UVAGmax}$) is 11 μm under UVAG. Meanwhile, the profile grinding process of UVAG is subjected to alternating grinding forces, which can cause micro-breakage in the abrasive grains. However, according to Cao et al., this does not compromise their ability to maintain sharpness and excellent form accuracy on formed surfaces [36].

Figure 10 illustrates the surface morphologies of the root and tip of the workpiece post-machining with optimized parameters. The grinding texture on the root surface is more distinct than that on the tip surface under both grinding processes, as shown in Fig. 10a and c compared to Fig. 10b and d. The mechanical interaction between the abrasive grit and the workpiece surface is more pronounced in the convex arc of the grinding wheel due to a greater amount of material removal required compared to that in the concave arc [37]. Deep abrasion marks tend

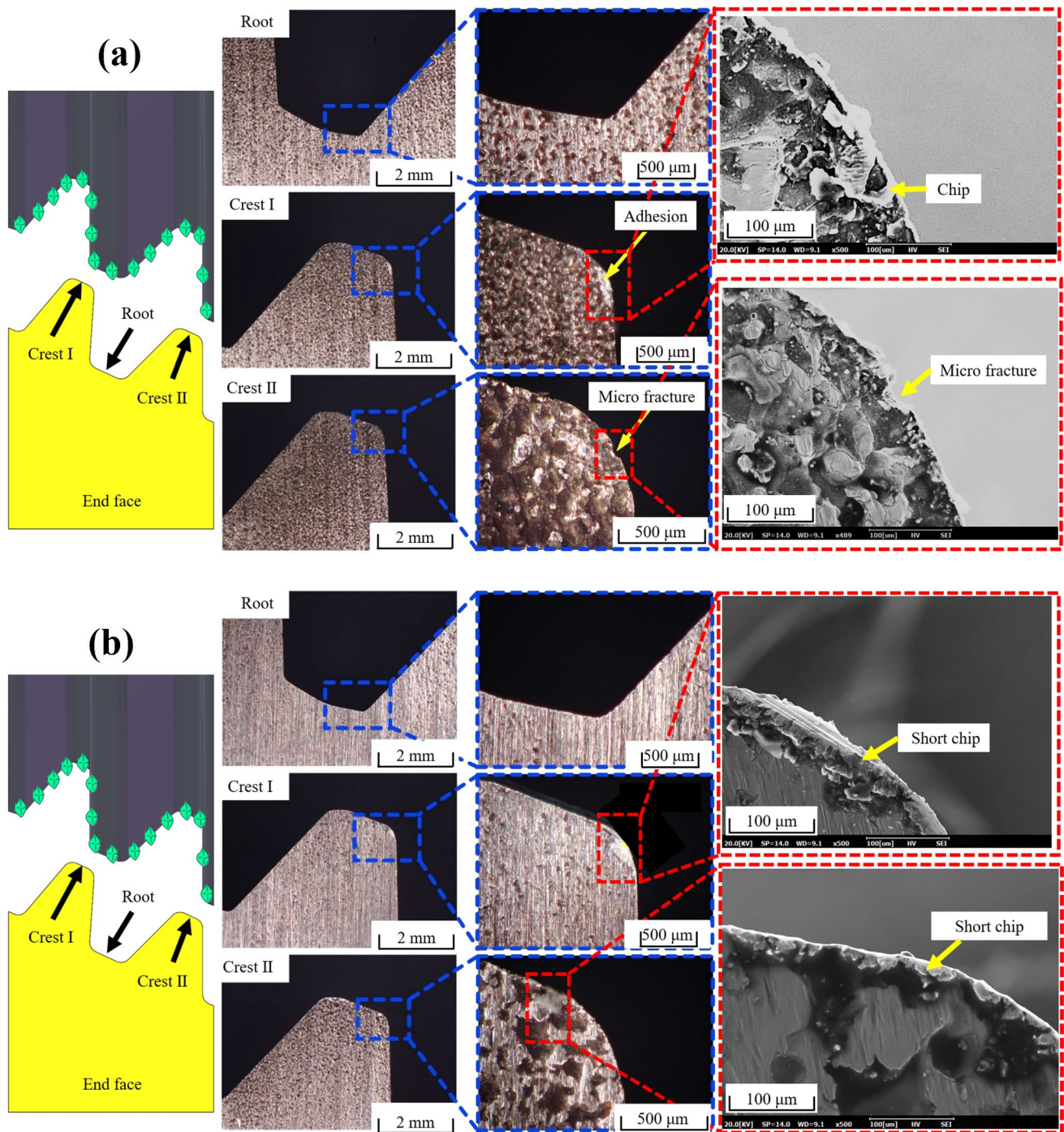**Fig. 7** Diagram of MOPSO particle change and table of Pareto solution

v_s/(m·s⁻¹)	v_w/(m·min⁻¹)	a_p/μm	Optimal value	
			F_n/N	R_a/μm
30.00	6.01	25.00	142.67	0.357
30.00	6.51	23.08	140.59	0.360
30.00	6.62	22.69	140.15	0.361
30.00	6.96	21.72	139.65	0.363
30.00	7.15	21.08	138.60	0.364
30.00	7.55	20.15	138.30	0.366
30.00	7.74	19.60	137.32	0.367
30.00	8.21	18.65	136.98	0.369
30.00	8.45	17.88	134.62	0.370
30.00	8.48	17.79	134.36	0.370
30.00	8.80	17.08	133.09	0.371
30.00	9.35	16.09	131.69	0.373
30.00	9.83	15.45	131.55	0.375
29.97	9.93	15.16	130.42	0.375
29.95	10.00	15.02	130.05	0.375

Fig. 8 Surface morphology of workpiece end face with profile grinding of (**a**) CG and (**b**) UVAG

to form on the lower area of the workpiece, resulting in surface damage from material breakage even occurring on the CG root surface. In the tip region of the workpiece, material coating of the machined surface occurs due to heat accumulation during grinding and increased material plasticity in profile grinding of CG and UVAG.

The occurrence of pits is reduced under UVAG due to the ultrasonic vibration's ability to further decrease the workpiece material's hardness. These findings demonstrate the effectiveness of optimized parameters in producing shaped workpieces without fractured tooth edges or surface defects.

(a) Grinding coordinate system   (b) Grinding wheel wear   (c) Chips length and thickness
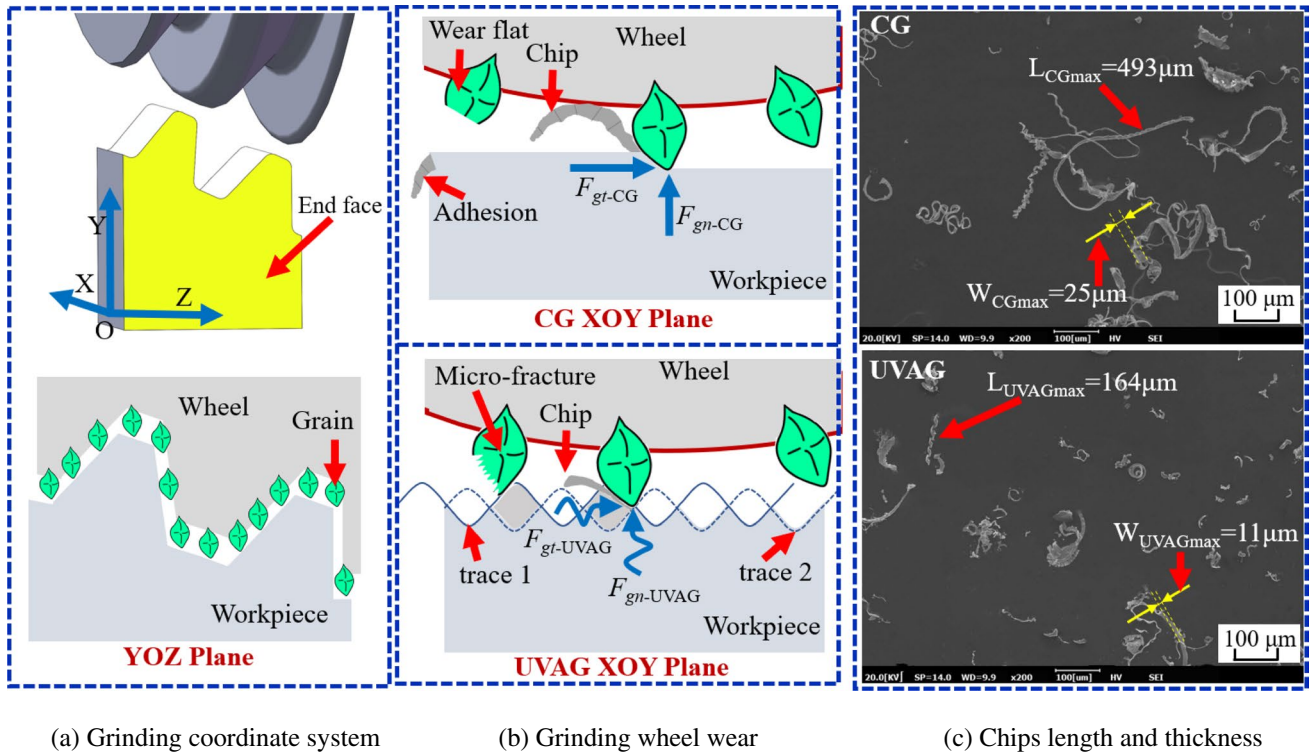
Fig. 9 Diagram depicting the coordinate of grinding wheel, wear of grinding wheel, and distribution of chips during profile grinding of CG and UVAG

(a) CG root surface

(b) CG tip surface

(c) UVAG root surface

(d) UVAG tip surface
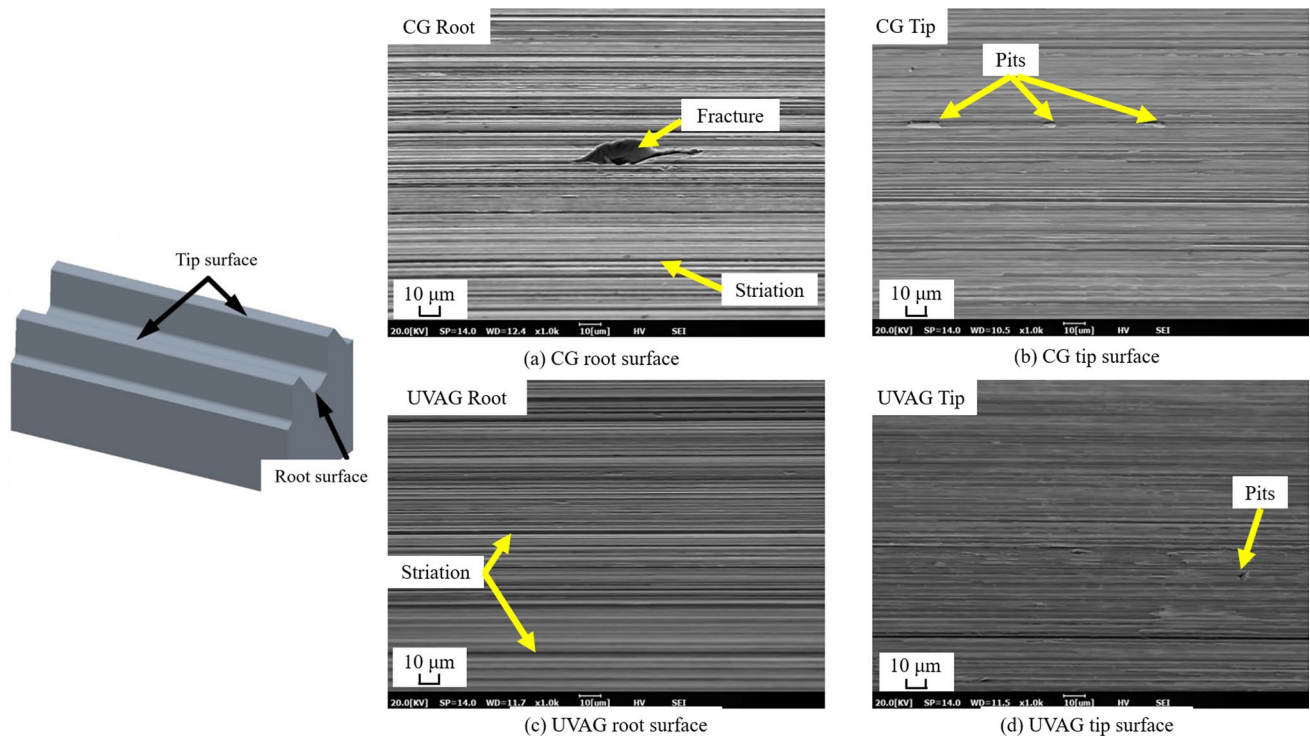
Fig. 10 Surface morphology of workpiece grinding face

5 Conclusions

Comparative experiments between CG and UVAG were conducted on hardened surfaces using white corundum wheels to investigate the effects of processing parameters on grinding forces and surface roughness. A multi-objective optimization model for grinding force and surface roughness profile was established using the MOPSO algorithm. The optimized parameters were used to conduct profile grinding experiments on curved parts under both CG and UVAG processes. The main conclusions are as follows:

1. The utilization of ultrasonic vibration resulted in an average reduction of 20.51% and 18.91% in tangential and normal grinding forces, respectively. Additionally, there was an average improvement of 9.47% in surface roughness quantities, while wheel wear was effectively reduced.

2. Empirical formulas established for grinding force and surface roughness demonstrated a 5% error margin in comparison to the measured values. The utilization of the MOPSO algorithm resulted in obtaining a Pareto solution set comprising of 15 noninferior solutions, indicating that optimal surface roughness can be achieved through larger wheel speed and depth of cut, coupled with smaller workpiece speed.

3. The optimized grinding parameters resulted in excellent shape accuracy and high surface quality of the formed workpiece, as the abrasive grains were maintained sharp and chips became shorter and narrower.

Data availability All data generated or analyzed during this study are included in the present article.

Declarations

Ethics approval The article follows the guidelines of the Committee on Publication Ethics (COPE) and involves no studies on human or animal subjects.

Consent to participate Not applicable.

Consent for publication Not applicable.

Competing interests The authors declare no competing interests.

References

1. Yang ZC, Zhu LD, Zhang GX, Ni CB, Lin B (2020) Review of ultrasonic vibration-assisted machining in advanced materials. Int J Mach Tools Manuf 156:103594

2. Zhang HT, Bao Y, Yang F, Sun HQ, Dong ZG, Kang RK (2022) Ultrasonic assisted helical grinding of SiC/SiC ceramic matrix composites. Diamond Abrasives Eng 42(1):81–87

3. Dong GJ, Wang L, Gao SD (2022) Grinding force model for rotary ultrasonic grinding of TiB$_w$ mesh reinforced titanium matrix composites. Diamond Abrasives Eng 42(1):97–102

4. Zhang MH, Pang ZX, Jia YX, Shan CW (2021) Understanding the machining characteristic of plain weave ceramic matrix composite in ultrasonic-assisted grinding. Ceram Int 48:5557–5573

5. Ning FD, Cong WL (2020) Ultrasonic vibration-assisted (UV-A) manufacturing processes: State of the art and future perspectives. J Manuf Process 51:174–190

6. Jamshidi H, Nategh MJ (2013) Theoretical and experimental investigation of the frictional behavior of the tool–chip interface in ultrasonic-vibration assisted turning. Int J Mach Tools Manuf 65:1–7

7. Peng ZL, Zhang XY, Zhang DY (2021) Performance evaluation of high-speed ultrasonic vibration cutting for improving machinability of Inconel 718 with coated carbide tools. Tribol Int 155:106766

8. Gao HH, Ma BJ, Zhu YP, Yang H (2022) Enhancement of machinability and surface quality of Ti-6Al-4V by longitudinal ultrasonic vibration-assisted milling under dry conditions. Measurement 187:110324

9. Juri AZ, Nakanishi Y, Yin L (2021) Microstructural influence on damage-induced zirconia surface asperities produced by conventional and ultrasonic vibration-assisted diamond machining. Ceram Int 47:25744–25754

10. Wang H, Hu YB, Cong WL, Hu ZY, Wang WQ (2020) A novel investigation on horizontal and 3D elliptical ultrasonic vibrations in rotary ultrasonic surface machining of carbon fiber reinforced plastic composites. J Manuf Process 52:12–25

11. Zhao B, Guo XC, Bie WB, Chang BQ, Zhao CY (2020) Thermo-mechanical coupling effect on surface residual stress during ultrasonic vibration-assisted forming grinding gear. J Manuf Process 59:19–31

12. Cao Y, Zhu YJ, Ding WF, Qiu YT, Wang LF, Xu JH (2021) Vibration coupling effects and machining behavior of ultrasonic vibration plate device for creep-feed grinding of Inconel 718 nickel-based superalloy. Chin J Aeronaut 35:332–345

13. Yang ZQ, Huang Z, Wang LM, Yang H (2022) Process parameter optimization model for robotic abrasive belt grinding of aero engine blades. Journal of Advanced Manufacturing Technology. https://doi.org/10.1007/s00170-022-10626-0

14. Chen FY, Sun YL, Wang LY, Zhang P, Sheng Y, Nishikawa N (2022) Optimization of process parameters for finishing the bottom surface of inner groove by magnetic grinding. Diamond Abrasives Eng 42(2):216–222

15. Ren ZD, Li BZ, Zhou QZ, Hou RD, Zhang YW (2022) Optimization of high-speed grinding parameters for anti-fatigue performance of 20CrMnTi steel. J Adv Manuf Technol 122:3565–3581

16. Wang ZX, Zhang TQ, Yu TB, Zhao J (2020) Assessment and optimization of grinding process on AISI 1045 steel in terms of green manufacturing using orthogonal experimental design and grey relational analysis. J Clean Prod 253:119896

17. Mukherjee I, Ray PK (2006) A review of optimization techniques in metal cutting processes. Comput Ind Eng 50(1–2):15–34

18. Marler RT, Arora JS (2004) Survey of multi-objective optimization methods for engineering. Struct Multidiscip Optim 26(6):369–395

19. Khan AM, Jamil M, Pimenov DY (2018) Multi-objective optimization for grinding of AISI D2 steel with Al_2O_3 wheel under MQL. Materials 11(11):2269

20. Zhang YW, Li BZ, Yang JG, Liang S (2018) Modeling and optimization of alloy steel 20CrMnTi grinding process parameters based on experiment investigation. Int J Adv Manuf Technol 95:1859–1873

21. Zhou H, Ding WF, Li Z, Su HH (2019) Predicting the grinding force of titanium matrix composites using the genetic algorithm optimizing back-propagation neural network model. Proc Inst Mech Eng Part B: J Eng Manuf 233(4):1157–1167

22. Coello CC, Lechuga MS (2002) MOPSO: a proposal for multiple objective particle swarm optimization. In Proceedings of the 2002 Congress on Evolutionary Computation. CEC'02 (Cat. No. 02TH8600) (Vol. 2, pp. 1051–1056). IEEE.

23. Petchrompo S, Coit DW, Brintrup A, Wannakrairot A, Parlikad AK (2022) A review of Pareto pruning methods for multi-objective optimization. Computer and Industrial Engineering 167:108022

24. Xiao GD, Zhao B, Ding WF, Huan HX (2021) On the grinding performance of metal-bonded aggregated cBN grinding wheels based on open-pore structures. Ceram Int 47:19709–19715

25. Wang W, Zhang Z, Yao P, Wang XY, Wang XG, Zhang ZB, Liu YH (2021) Envelope grinding of micro-cylinder array lenses using a near arc-profile wheel without on-machine precision truing. J Mater Process Technol 289:116927

26. Taghi T, Bahman A (2008) Influence of ultrasonic vibrations on dry grinding of soft steel. Int J Mach Tools Manuf 48:1585–1591

27. Cao Y, Zhu YJ, Li HN, Wang CX, Su HH, Yin Z, Ding WF (2020) Development and performance of a novel ultrasonic vibration plate sonotrode for grinding. J Manuf Process 57:174–186

28. Wu BF, Zhao B, Ding WF (2021) Investigation of the wear characteristics of microcrystal alumina abrasive wheels during the ultrasonic vibration-assisted grinding of PTMCs. Wear 477:203844

29. Jeffery B, Stuart M, Garret EO (2021) Big-and-dull or small-and-sharp: a comparison of specific energy, wheel wear, surface-generation mechanisms and surface characteristics when grinding with Al_2O_3 and CBN to achieve a given surface roughness. J Mater Process Technol 288:116825

30. Jin T, Stephenson DJ, Xie GZ, Sheng XM (2011) Investigation on cooling efficiency of grinding fluids in deep grinding. CIRP Annal Manuf Technol 60:343–346

31. Cao Y, Yin JF, Ding WF, Xu JH (2021) Alumina abrasive wheel wear in ultrasonic vibration-assisted creep-feed grinding of Inconel 718 nickel-based superalloy. J Mater Process Technol 297:117241

32. Zhang DK, LI CH, Jia DZ, Zhang YB, Zhang XW (2015) Specific grinding energy and surface roughness of nanoparticle jet minimum quantity lubrication in grinding. Chin J Aeronaut 28(2):570–581

33. Tao HF, Liu YH, Zhao DW, Lu XC (2022) Undeformed chip width non-uniformity modeling and surface roughness prediction in wafer self-rotational grinding process. Tribol Int 171:107547

34. Ni CB, Zhu LD (2022) Investigation on machining characteristics of TC4 alloy by simultaneous application of ultrasonic vibration assisted milling (UVAM) and economical-environmental MQL technology. J Mater Process Technol 278:116518

35. Xiao YL, Wang SL, Ma C, Wang SB, Yang WH, Xia CJ, Wang J (2022) Numerical modeling of material removal mechanism and surface topography for gear profile grinding. J Manuf Process 76:719–739

36. Cao Y, Zhao B, Ding WF, Liu YC, Wang LF (2021) On the tool wear behavior during ultrasonic vibration-assisted form grinding with alumina wheels. Ceram Int 47:26465–26474

37. Guerrini G, Lerra F, Fortunato A (2019) The effect of radial infeed on surface integrity in dry generating gear grinding for industrial production of automotive transmission gears. J Manuf Process 45:234–241